



## A global, multi-scale simulation of laminar fluid mixing: the extended mapping method

Oleksiy S. Galaktionov<sup>a</sup>, Patrick D. Anderson<sup>a</sup>, Gerrit W. M. Peters<sup>a</sup>,  
Charles L. Tucker III<sup>b,\*</sup>

<sup>a</sup> *Materials Technology, Eindhoven University of Technology, 5600 MB Eindhoven, The Netherlands*

<sup>b</sup> *Department of Mechanical and Industrial Engineering, University of Illinois at Urbana-Champaign, Urbana, IL 61801, USA*

Received 7 November 2000; received in revised form 26 October 2001

---

### Abstract

We present a global, multi-scale model of fluid mixing in laminar flows, which describes the evolution of the spatial distribution of coarse-grain concentration and interfacial area in a mixture of two fluids with identical viscosity with no interfacial tension. This results in an efficient computational tool for mixing analysis, able to evaluate mixing dynamics and identify mixing problems such as dead zones (islands), applicable to realistic mixing devices. The flow domain is divided into cells, and large-scale variations in composition are tracked by following the cell-average concentrations of one fluid, using the mapping method developed previously. Composition fluctuations smaller than the cell size are represented by cell values of the area tensor which quantifies the amount, shape, and orientation of the interfacial area within each cell. The method is validated by comparison with an explicit interface tracking calculation. We show examples for 2D, time-periodic flows in a lid-driven rectangular cavity. The highly non-uniform time evolution of the spatial distribution of interfacial area can be determined with very low computational effort. Cell-to-cell differences in interfacial area of three orders of magnitude or more are found. It is well known that, for globally chaotic flows, the microstructural pattern becomes self-similar, and interfacial area increases exponentially with time. This behavior is also captured well by the extended mapping method. The present calculations are 2D, but the method can readily be applied in 3D problems. © 2002 Elsevier Science Ltd. All rights reserved.

*Keywords:* Mixing; Laminar mixing; Chaotic mixing; Chaotic flow; Area tensor; Microstructural mixing; Distributive mixing; Mapping method

---

---

\* Corresponding author. Tel.: +1-217-333-2692; fax: +1-217-244-6534.  
*E-mail address:* c-tucker@uiuc.edu (C.L. Tucker III).

## 1. Introduction

Laminar chaotic mixing of viscous fluids is fundamentally important, universally practiced, and has been extensively studied in the last 15–20 years. Yet we lack a general ability to predict the outcome of any particular realistic mixing operation. Dynamical systems and chaos theories provide fundamental understanding of the laminar mixing process in terms of Poincaré sections, periodic points, related stable and unstable manifolds, self-similarity and asymptotic directionality (Ottino, 1989; Muzzio et al., 1991, 2000; Meleshko, 1996; Giona et al., 1999). The majority of the mixing systems analyzed in this way are idealized, relatively simple flows such as the blinking vortex system (Aref, 1984; Khakhar et al., 1986), the tendril-whorl flow (Aref, 1984), flow between eccentric cylinders (Aref and Balachandar, 1986; Swanson and Ottino, 1990) and the lid-driven cavity flow (Liu et al., 1994b; Meleshko and Peters, 1996; Giona et al., 1999).

When looking at more realistic mixing processes, it is desirable to express the dynamics of the mixing process and state of the mixture in terms of other mixing properties such as distributions of concentration, residence time and interfacial area. Moreover, there is a strong need for an efficient method for analyzing realistic mixing processes. Such a method should be able to handle the geometrical complexity of commercial mixing devices, and assess both short- and long-term mixing performance. Ultimately, the goal is to be able to optimize any mixing process or device.

A tool that offers many of these features is the mapping method, a scheme whose merits and limitations have been demonstrated by studying the concentration distribution in the lid-driven cavity flow (Kruijt, 2000; Kruijt et al., 2001a). The mapping method is based on discretizing the mixing domain (subdividing the domain into cells) and determining a distribution mapping matrix related to the discretized space. Determining the mapping matrix can be computationally expensive; however, once mapping matrix has been composed, the use of the mapping method requires only modest computational effort. Kruijt et al. (2001c) and Kruijt (2000) show that the method can treat the dynamics of the concentration distribution in a fully filled co-rotating twin screw extruder. This extruder problem involves a 3D domain with complex, time-dependent geometry, and continuous flow through the mixer.

In this paper we extend the mapping method to model the dynamic growth, spatial distribution, and orientation of the interfacial area during liquid–liquid mixing. Concentration fluctuations on a scale smaller than the cell size, i.e. the microstructure of the mixture, are represented by an area tensor (Wetzel and Tucker, 1999), which describes the interfacial area per unit volume and its orientation. Thus, the method treats the mixing process at multiple length scales, across the entire mixing domain. The distinction between macrostructural and microstructural features of the mixture is made at the computational cell size, a dividing line that is arbitrary but convenient.

In this paper we focus on a 2D flow, the lid-driven cavity, but the method is readily generalized to 3D. The present model is limited to passive mixing, where the two fluids have identical rheology and zero interfacial tension, and where diffusion is negligible. More complicated models for droplet dispersions can incorporate the dynamics of deformation, breakup, and coalescence of the droplets, together with local average concentrations (Peters et al., 2001), and these models are philosophically similar to the present model.

This paper is organized as follows. Section 2 reviews the main features of the original mapping calculation and the area tensor. Section 3 then describes the extended mapping method and its numerical implementation. Section 4 presents results for 2D time-periodic flows in a lid-driven

cavity. Here we examine flows that are globally chaotic, as well as flows with large regular islands. The information provided by the extended mapping method is compared to the information provided by some classical tools of chaos analysis. We also examine self-similarity in the microstructure in chaotic flows, the spatial distribution of interfacial area growth, and artifacts of the numerical method. The paper finishes with a discussion and summary.

## 2. Background

### 2.1. The mapping method

Consider a batch mixing device that uses a time-periodic flow field. In the original mapping method (Kruijt et al., 2001a), the flow domain  $\Omega$  is divided into  $N$  non-overlapping sub-domains  $\Omega_i$  with boundaries  $\partial\Omega_i$ . The coarse-grain concentration  $C_i$  within each cell is defined as

$$C_i = \frac{1}{\Omega_i} \int_{\Omega_i} c \, d\Omega_i \quad (1)$$

and the column vector containing all the cell values at time  $t_k$  is  $\{C\}^k$ . The mapping method advances these values over large, discrete time steps using a matrix multiplication

$$C_i^{k+1} = \sum_{j=1}^N \Psi_{ij} C_j^k, \quad (2)$$

where  $[\Psi]$ , called the *mapping matrix*, is constructed using the velocity field in the flow domain and an accurate adaptive interface tracking algorithm.

To understand the construction of  $[\Psi]$ , consider a 2D cavity flow, where the motion is created by translating either the upper or the lower surface. The geometry of this flow is shown in Fig. 1. In Fig. 1(a) we see the initial grid of cells. The cell boundaries  $\partial\Omega_i$  are tracked from time  $t_k$  to  $t_{k+1} = t_k + \Delta t$  using an adaptive interface tracking method (Galaktionov et al., 2000a), to produce the deformed grid in Fig. 1(b). This deformed grid is then laid over the initial grid, and each

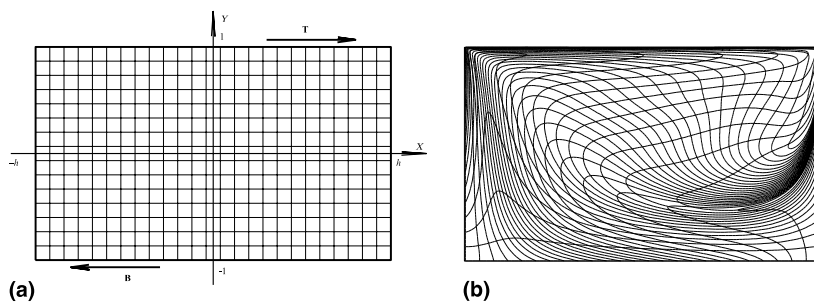


Fig. 1. (a) Geometry of the cavity flow (the side walls are fixed, while the top and bottom walls can translate horizontally) and initial sub-domain discretization ( $25 \times 15$  grid) in a cavity. (b) Deformed grid after displacing the top wall by two times its length. During the actual computations a finer grid ( $200 \times 120$ ) was used.

matrix component  $\Psi_{ij}$  is computed as the area of overlap between deformed cell  $j$  and undeformed cell  $i$ , divided by the total area of cell  $j$ :

$$\Psi_{ij} = \frac{\int_{\Omega_j|_{t_{k+1}} \cap \Omega_i|_{t_k}} d\Omega}{\int_{\Omega_j|_{t_k}} d\Omega}. \quad (3)$$

The matrix  $[\Psi]$  can be very large, but it is typically quite sparse, so with careful programming the multiplications of Eq. (2) can be done quite rapidly. Calculation of the mapping matrix  $[\Psi]$  is an expensive step. However, this matrix is calculated once, off-line, and the results are stored for later use.

If each cell contains only one kind of fluid (each  $C_i$  equals either 1 or 0), then the results of a single mapping step are exact. If we think of the two fluids as being black and white, some cells become gray, because they receive black fluid from some donors and white fluid from others. This is exactly the physical process we wish to capture at the macroscale. On the second and subsequent mapping steps, small errors appear. If a donor cell contains both black and white fluid at the beginning of the step, the exact solution may be that the black fluid goes to one recipient cell and the white fluid to another. However, the mapping calculation only knows the average concentration in the cell, so it transfers this mixture of black and white fluid to every recipient cell. This introduces numerical diffusion, providing a second, non-physical mechanism by which the cell concentrations become more uniform. Numerical diffusion is known to affect the quantitative results of the mapping method (Kruijt et al., 2001a; Tucker and Peters, submitted), and we will see that it has a similar effect in the extended mapping method. We minimize numerical diffusion effects by making the time steps as large as possible. However, if the time step becomes too large, then  $[\Psi]$  is too expensive to compute, and too densely populated to use effectively.

## 2.2. Area tensors and their evolution

Interfacial area has long been recognized as an important measure of the fine-scale structure of a mixture (Spencer and Wiley, 1951; Mohr et al., 1957). Popular measures for lamellar mixtures are the interfacial area per unit volume  $S_V$  and the local average striation thickness  $\lambda$ . These are related by

$$\lambda = \frac{2}{S_V}. \quad (4)$$

Neither  $\lambda$  nor  $S_V$  are adequate descriptors for our present purposes, because one cannot calculate their change for a given deformation without additional information – in this case the orientation of the interface.

A useful generalization of the interfacial area measure, which includes orientation, is the *area tensor* (Wetzel and Tucker, 1999). Consider a small averaging volume  $V$ , and let  $\Gamma$  represent the interfacial surface lying within this volume (see Fig. 2). Let  $\mathbf{n}$  denote the unit normal vector for any incremental area  $d\Gamma$ .

The second-order area tensor  $\mathbf{A}$  is defined as

$$\mathbf{A} = \frac{1}{V} \int_{\Gamma} \mathbf{nn} \, d\Gamma. \quad (5)$$

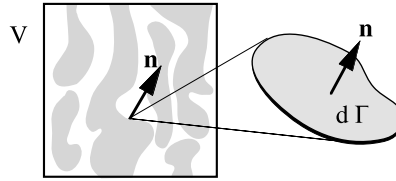


Fig. 2. Averaging volume  $V$ , containing the interfacial surface  $\Gamma$ . For each increment of surface  $d\Gamma$  the unit normal vector is  $\mathbf{n}$ .

The components of the area tensor have units of interfacial area per unit volume, or  $(\text{length})^{-1}$  and the trace of the tensor equals the total interfacial area per unit volume

$$\text{tr } \mathbf{A} = S_V, \tag{6}$$

so  $\text{tr } \mathbf{A}$  is a useful scalar measure of microstructural mixing. The averaging volume  $V$  should be large enough to provide a representative sample of the microstructure, but smaller than the scale over which the microstructure varies. In previous work (Wetzel and Tucker, 1999) this volume was never chosen explicitly.

The area tensor captures information about the size, shape, and orientation of the microstructure. Table 1 shows the area tensors for three particular microstructures. These three examples are limiting cases, and the area tensor can represent any intermediate structure as well, such as a group of identical ellipsoidal droplets. The interfacial area of a non-spherical droplet is distributed non-uniformly in space, and this is captured by the area tensor. The principal axes of the tensor will also be co-axial with the principal axes of the droplet, so the area tensor describes the droplet orientation. Any other microstructure that possesses a distinct interface also possesses an area tensor, so even complex structures like co-continuous morphologies can be represented.

The area tensor, or its isotropic and deviatoric parts, determines the contribution of interfacial tension to bulk stress (Batchelor, 1970; Onuki, 1987), and has been used as the state variable in rheological theories of polymer blends (Doi and Ohta, 1991; Grmela and Ait-Kadi, 1998; Wagner et al., 1999; Peters et al., 2001). Thus, the area tensor has a sound theoretical basis as a microstructural variable.

For passive mixing, each part of the interface  $d\Gamma$  deforms affinely with the material. This can be used to derive a differential evolution equation for the area tensor (Wetzel and Tucker, 1999):

$$\dot{\mathbf{A}} = -\mathbf{L}^T \cdot \mathbf{A} - \mathbf{A} \cdot \mathbf{L} + \mathbf{L} : \mathbb{A}. \tag{7}$$

In this equation the dot indicates a material derivative, and  $L_{ij} = \partial u_i / \partial x_j$  is the velocity gradient tensor.  $\mathbb{A}$  is the fourth-order area tensor, defined as

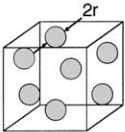
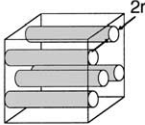
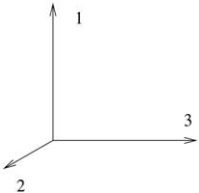
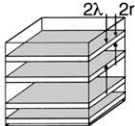
$$\mathbb{A} = \frac{1}{V} \int_{\Gamma} \mathbf{n} \mathbf{n} \mathbf{n} \mathbf{n} d\Gamma. \tag{8}$$

This must be replaced by a closure approximation, giving  $\mathbb{A}$  in terms of  $\mathbf{A}$ , to have a closed evolution equation. The simplest example is the quadratic closure (Doi and Ohta, 1991),

$$\mathbb{A} = \frac{\mathbf{A} \mathbf{A}}{\text{tr } \mathbf{A}}. \tag{9}$$

Table 1

Three microstructures and their corresponding area tensors. Adapted from Wetzel and Tucker (1999)

Geometry		$\mathbf{A}$	
Spherical		$S_V \begin{bmatrix} \frac{1}{3} & 0 & 0 \\ 0 & \frac{1}{3} & 0 \\ 0 & 0 & \frac{1}{3} \end{bmatrix}$	
Cylindrical		$S_V \begin{bmatrix} \frac{1}{2} & 0 & 0 \\ 0 & \frac{1}{2} & 0 \\ 0 & 0 & 0 \end{bmatrix}$	
Lamellar		$S_V \begin{bmatrix} 1 & 0 & 0 \\ 0 & 0 & 0 \\ 0 & 0 & 0 \end{bmatrix}$	

A more accurate closure approximation can be constructed by assuming that the interface was, at some time, oriented isotropically in space (Wetzel and Tucker, 1999). Subsequent deformations will produce a distribution of interface orientation equivalent to a set of identical ellipsoidal droplets. Any set of identical ellipsoidal droplets possesses a unique combination of second- and fourth-order area tensors  $\mathbf{A}$  and  $\mathbb{A}$ . The closure based on this correspondence is called the rational ellipsoidal (RE) closure because it uses a rational polynomial approximation for the area tensor components associated with ellipsoidal droplets. Using a closure approximation, Eq. (7) can be integrated for any type of deformation. When the RE closure is used, the results are extremely accurate (Wetzel and Tucker, 1999).

### 3. The extended mapping method

#### 3.1. Area tensor transformation under finite deformation

In the original mapping method, the cell concentrations  $C_i$  describe the macrostructure, and we extend this by adding cell values of the area tensor to represent the microstructure. The mapping method takes large time steps, and we must develop a computation analogous to Eq. (2) for the area tensor. The mapping matrix  $[\Psi]$  accounts for advective transport of the microstructure, corresponding to the material derivative on the left-hand side of Eq. (7). The right-hand side of that equation represents the stretching and reorientation of area caused by fluid deformation, and

we must also account for this. Because the time step in the mapping calculation is large, the differential form of Eq. (7) is not suitable, and we seek an equivalent form for finite deformations.

Consider a material volume,  $V_0$  in some reference state, that is transformed by a finite deformation into the material volume  $V$ . Let  $\mathbf{x}^0$  denote the material coordinates, which equal the spatial coordinates  $\mathbf{x}$  in the reference configuration. The deformation between  $V_0$  and  $V$  is described by the deformation gradient tensor

$$\mathbf{F} = \frac{\partial \mathbf{x}}{\partial \mathbf{x}^0} \tag{10}$$

and we assume that  $\mathbf{F}$  is uniform over the material volume  $V^0$ .

Let  $\mathbf{n}^0$  denote the unit vector normal to the interface  $dI^0$  in the reference configuration. The transformations of  $\mathbf{n}^0$  and  $dI^0$  under finite deformation are well known, e.g. (Wetzel and Tucker, 1999)

$$\frac{dI}{dI^0} = \det \mathbf{F} \sqrt{(\mathbf{F}^T \cdot \mathbf{F})^{-1} : \mathbf{n}^0 \mathbf{n}^0}, \tag{11}$$

$$\mathbf{n} = \frac{(\mathbf{F}^{-1})^T \cdot \mathbf{n}^0}{\sqrt{(\mathbf{F}^T \cdot \mathbf{F})^{-1} : \mathbf{n}^0 \mathbf{n}^0}}. \tag{12}$$

Simply substituting these into Eq. (5) gives

$$\mathbf{A} = (\det \mathbf{F})(\mathbf{F}^{-1})^T \cdot \left( \frac{1}{V} \int_I \frac{\mathbf{n}^0 \mathbf{n}^0}{\sqrt{(\mathbf{F}^T \cdot \mathbf{F})^{-1} : \mathbf{n}^0 \mathbf{n}^0}} dI^0 \right) \cdot \mathbf{F}^{-1}. \tag{13}$$

The right-hand side of this equation cannot be manipulated to contain only  $\mathbf{F}$  and the area tensor in the reference state  $\mathbf{A}^0$ , hence there is no universal relationship of the type we seek. Instead, some approximation is essential.

The approximation used here is based on the same idea as the RE closure: to any area tensor  $\mathbf{A}$  and second-phase volume fraction  $\phi$ , there corresponds a unique set of identical ellipsoidal droplets. The size, shape and orientation of the droplets can be characterized by a droplet shape tensor  $\mathbf{G}$  (Wetzel and Tucker, 2001; Wetzel, 1999). This tensor is defined such that, if the center of the droplet is at the origin, points on the droplet surface satisfy the equation

$$\mathbf{x} \cdot \mathbf{G} \cdot \mathbf{x} = 1. \tag{14}$$

To obtain the transformation law for  $\mathbf{G}$  under finite strain we first note that in the reference configuration the points on the droplet surface satisfy

$$\mathbf{x}^0 \cdot \mathbf{G}^0 \cdot \mathbf{x}^0 = 1. \tag{15}$$

Using Eq. (10) to replace  $\mathbf{x}^0$  by  $\mathbf{x}$ , we have, in the deformed configuration,

$$\mathbf{x} \cdot \left( (\mathbf{F}^{-1})^T \cdot \mathbf{G}^0 \cdot \mathbf{F}^{-1} \right) \cdot \mathbf{x} = 1. \tag{16}$$

Comparing this to Eq. (14) we see that the term in parentheses equals  $\mathbf{G}$ , so the finite-strain transformation rule is simply

$$\mathbf{G} = (\mathbf{F}^{-1})^T \cdot \mathbf{G}^0 \cdot \mathbf{F}^{-1}. \quad (17)$$

Our route for transforming the area tensor under finite strain is to convert the initial area tensor  $\mathbf{A}^0$  to an equivalent droplet shape tensor  $\mathbf{G}^0$ , find  $\mathbf{G}$  in the deformed state using Eq. (17), and then transform  $\mathbf{G}$  back to find the deformed-state area tensor  $\mathbf{A}$ . As a notational convenience we write this transformation as

$$\mathbf{A} = \mathbf{A}^0 \otimes \mathbf{F}^{-1}. \quad (18)$$

The details of the conversion between  $\mathbf{A}$  and  $\mathbf{G}$  are shown in Appendix C.

### 3.2. Algorithm

In the extended mapping method, the cell volume  $\Omega_i$  serves as the averaging volume for the area tensor. For cell  $i$  the associated area tensor is

$$\mathbf{A}_i = \frac{1}{\Omega_i} \int_{\Gamma_i} \mathbf{nn} \, d\Gamma. \quad (19)$$

Here  $\Gamma_i$  is the interfacial surface lying within  $\Omega_i$ . Because  $\Omega_i$  is explicitly chosen and has finite volume, the cell area tensor  $\mathbf{A}_i$  is a coarse-grain variable, like  $C_i$ .

For each non-zero entry  $\Psi_{ij}$  in the mapping matrix, we compute an inverse deformation gradient tensor  $\mathbf{F}_{ij}^{-1}$ . This is evaluated at the centroid of  $\Omega_j|_{t_{k+1}} \cap \Omega_i|_{t_k}$ , the intersection between the deformed cell  $j$  and the undeformed cell  $i$ . This computation is carried out off-line, at the same time the mapping matrix  $[\Psi]$  is being computed, and the results are stored for later use. Appendix B discusses the details of this computation.

The extended mapping method updates the area tensor at each time step according to

$$\mathbf{A}_i^{k+1} = \sum_{j=1}^N \Psi_{ij} \left( \mathbf{A}_j^k \otimes \mathbf{F}_{ij}^{-1} \right). \quad (20)$$

That is, the area tensor in any cell at time  $k + 1$  is the sum of contributions from all donor cells, after the donor tensors from time  $k$  have been transformed by the appropriate deformation gradients. Eqs. (20) and (2) constitute one step of the extended mapping method.

The extended mapping method takes advantage of a key characteristic of the area tensor: it is additive. More precisely, if a domain  $\Omega$  is the union of two non-overlapping sub-domains  $\Omega_1$  and  $\Omega_2$ , and if the area tensors associated with the sub-domains are  $\mathbf{A}_1$  and  $\mathbf{A}_2$ , then the area tensor for the whole domain is

$$\begin{aligned} \mathbf{A} &= \frac{1}{\Omega} \int_{\Gamma} \mathbf{nn} \, d\Gamma \\ &= \frac{1}{\Omega_1 + \Omega_2} \left[ \int_{\Gamma_1} \mathbf{nn} \, d\Gamma_1 + \int_{\Gamma_2} \mathbf{nn} \, d\Gamma_2 \right] \\ &= \left( \frac{\Omega_1}{\Omega_1 + \Omega_2} \right) \mathbf{A}_1 + \left( \frac{\Omega_2}{\Omega_1 + \Omega_2} \right) \mathbf{A}_2. \end{aligned} \quad (21)$$



That is, the area tensor for any domain is the sum of the area tensors its sub-domains, weighted by the fraction of volume they occupy. This property of the area tensor allows us to sum the contributions from the donor cells in Eq. (20). Other microstructural descriptors, such as the droplet shape tensor  $\mathbf{G}$ , do not have this additive property, and cannot be used in the same way.

Eq. (20) assumes that the deformation gradient  $\mathbf{F}^{-1}$  is uniform over the intersection between each deformed and undeformed cell. In general this approximation will be accurate if the cell size is small enough. In the present calculations, which concern flow in a lid-driven cavity, the approximation is excellent over most of the flow domain. The largest errors arise when the deformed cell has passed close to one of the corner singularities during the time step.

To illustrate the magnitude of the errors of the numerical evaluation of  $\mathbf{F}^{-1}$ , its determinant is evaluated. The RMS deviation  $\epsilon$  of the determinant of the deformation gradient from its ideal value of 1.0 is computed over all intersections of deformed and undeformed cells, for the different values of dimensionless wall displacement used in this study. These results are summarized in Table 2. The maximum error occurs, as expected, for the flow with the largest wall displacement,  $D = 4$ . In this case there are a few cell intersections where the deformed cell has traveled close to both corner singularities. In these (few) cases,  $\det(\mathbf{F}^{-1})$  reaches absolute minimum and maximum values of 0.9658 and 1.0107, respectively. Note that  $\det(\mathbf{F}^{-1}) = 1$  is a necessary, but not sufficient, condition for accurate computation of the deformation gradient tensor.

Since advection of the microstructure is handled the same way as advection of the concentration, it will be subject to the same type of numerical diffusion. We will explore the nature and magnitude of this error in the calculations.

### 3.3. Implementation

In this paper we study the 2D time-periodic Stokes flow in a lid-driven cavity, as shown in Fig. 1. Many aspects of this flow have been studied, both theoretically and experimentally (Chien et al., 1986; Leong and Ottino, 1989; Ottino, 1989; Liu et al., 1994b,a; Meleshko and Peters, 1996; Giona et al., 1999; Kruijt et al., 2001a). We use the same geometry as many of these other studies, with a width to height ratio of 5:3.

In the present study we focus on the TB (top/bottom) protocol, originally considered by Franjione et al. (1989). Each period consists of two steps: first the top wall moves to the right, then the bottom wall moves to the left by the same amount. The displacement during of one step, scaled by the half-width of the cavity  $h$  (see Fig. 1), is denoted by  $D$ . The displacement of one wall during a period characterizes a particular protocol.

We use a semi-analytical solution for the velocity field (Meleshko, 1996; Meleshko and Gommilko, 1997). This solution is computationally efficient and gives accurate results in the whole domain, including the neighborhood of the corners.

Table 2  
RMS deviation  $\epsilon$  of  $\det(\mathbf{F}^{-1})$  from unity, for different values of dimensionless wall displacement  $D$

$D$	0.25	0.5	1.0	2.0	4.0
$\epsilon$	$5.54 \times 10^{-7}$	$1.11 \times 10^{-6}$	$2.05 \times 10^{-6}$	$6.11 \times 10^{-6}$	$1.38 \times 10^{-4}$

For the mapping calculations, a grid of  $120 \times 200$  rectangular cells covers the interior of the cavity. The interior cells extend from  $-0.995h < x < 0.995h$  and  $-0.999 < y < 0.999$ , leaving a single, very thin cell around the boundary. This boundary cell reduces computational expense, by avoiding the necessity to track points that pass very close to the corner singularities. When plotting results we show only the 24,000 interior cells, but when computing total quantities for the entire cavity we include the boundary cell.

There is no difficulty computing  $\Psi_{ij}$  for the boundary cell, so mapping of the concentrations proceeds using Eq. (2) for all cells. The area tensors for all interior cells are updated using Eq. (20). However, we cannot compute  $\mathbf{F}_{ij}^{-1}$  for material that enters or leaves the boundary cell, so special treatment is required. When the boundary cell is a recipient, we use  $\mathbf{F}_{ij}^{-1} = \mathbf{I}$  (the identity tensor), which transports interfacial area but ignores its stretching and reorientation. Since the correct orientation of interfaces leaving the boundary cell is not known, a reasonable option is to imply that the material coming from the boundary cell has an isotropic area tensor. To achieve this, after each mapping step, the area tensor corresponding to the boundary cell is symmetrized (replaced by an isotropic tensor with an equal trace). When the boundary cell is a donor, we again use the assumption  $\mathbf{F}_{ij}^{-1} = \mathbf{I}$ . Thus, recipient inner cell receives an isotropic contribution to its area tensor from the boundary cell. Numerical experiments show that this treatment of the boundary cell has a negligible effect on the overall results.

The mapping components  $\Psi_{ij}$  and the deformation measures  $\mathbf{F}_{ij}^{-1}$  are computed using an adaptive interface tracking scheme (Galaktionov et al., 2000a) for  $D = 0.25, 0.5, 1, 2,$  and  $4$ . This allows us to model any flow in which the wall motion is an integer multiple of  $0.25$ , by using multiple mapping steps to simulate a single step of wall motion. Motion of the bottom wall is treated using the symmetry of the flow, rather than by generating new mapping matrices and deformation tensors.

The computation of  $\Psi_{ij}$  and  $\mathbf{F}_{ij}^{-1}$  is quite involved, and took approximately 10 h on 14 processors (R10K) using SGI Origin200 trademark workstations. However, once this data is computed and stored, the mapping calculations are quite rapid. Each simulation shown here requires but a few minutes on a single-processor workstation. A single matrix-vector multiplication, together with the corresponding area tensor transformations, require between 3 and 5 s on a single CPU. This makes the extended mapping method very useful for exploring the effects of different mixing protocols, or different initial configurations of the fluids.

## 4. Results

### 4.1. Comparison to interface tracking

To test the accuracy of the extended mapping method, we compare its results to an explicit interface tracking calculation (Galaktionov et al., 2000a). Such comparisons are only possible in the initial stage of mixing, when the tracking calculation is still affordable. Here we consider the TB protocol with  $D = 6.25$ . The cavity is initially filled with white fluid, and a small rectangular blob of black marker fluid is placed around a hyperbolic (unstable) periodic point. The initial location of this blob is indicated by the dashed line in Figs. 3(a) and (b). The boundary of the blob was tracked for five periods of the flow ( $D_{\text{tot}} = 62.5$ ). The tracking results were then superimposed

on the grid used by the mapping calculation, and used to calculate cell concentrations and cell area tensors. This provides a nearly exact result, against which the mapping results can be compared. In the initial condition for mapping, only the cells containing the blob had non-zero concentrations, and only cells containing the blob boundary had non-zero area tensors.

The results are compared in Fig. 3. The concentration distribution obtained by mapping, though influenced by numerical diffusion, closely matches the tracking results. A careful examination of Figs. 3(a) and (b) suggests that the numerical diffusion spreads the material more in the direction of local stretching, since sharp folds in the material are more elongated in the mapping result. Figs. 3(c) and (d) show the spatial distribution of the trace of area tensor, which measures

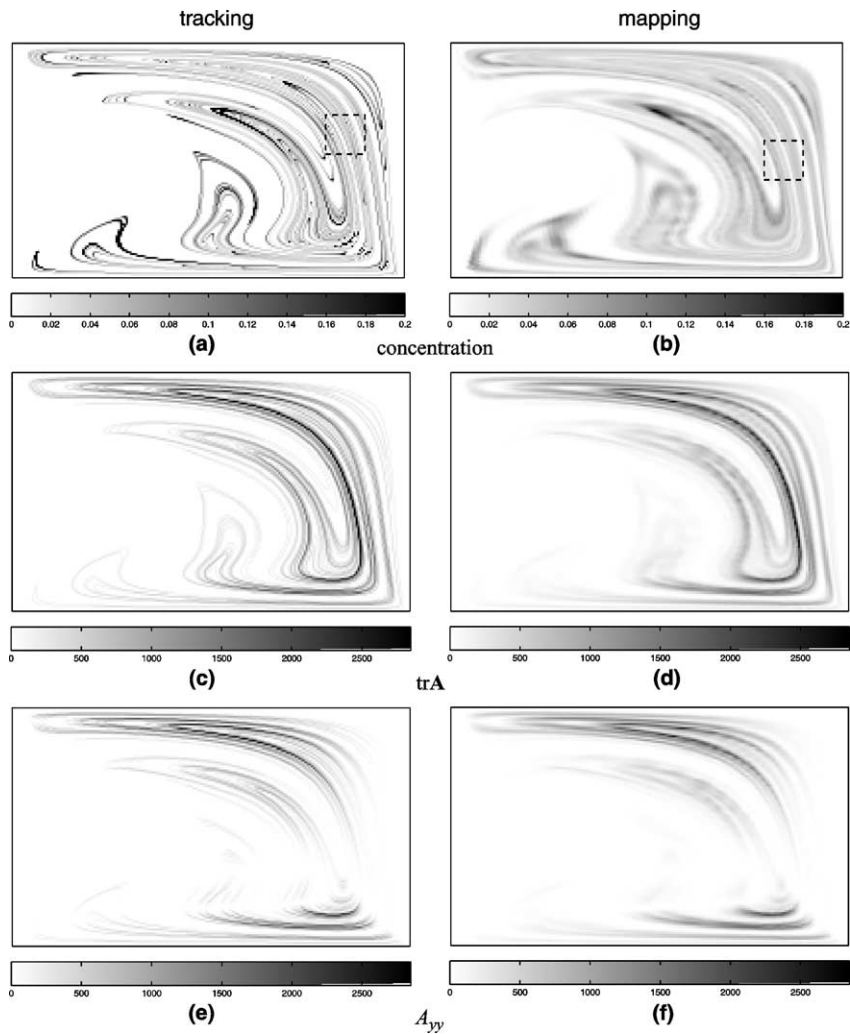


Fig. 3. Comparison of interface tracking (left) and mapping (right) results for advection of initially rectangular blob (indicated by the dashed line). Results for five periods of the TB protocol with  $D = 6.25$ : (a,b) concentration distribution (coarse grain density); (c,d) trace of the area tensor; (e,f)  $A_{yy}$  component of the area tensor.

the interfacial area per unit volume in each cell. Again, the mapping results are in good agreement with interface tracking. These figures are similar in appearance to the concentration patterns, mainly because there can only be interfacial area in a cell that contains some marker fluid. Values for the  $A_{yy}$  component of the area tensor are compared in Figs. 3(e) and (f), and again the comparison is good. Plotting  $A_{yy}$  emphasizes interfaces that are nearly horizontal, i.e., their normals point in the  $y$  direction. These figures look much like the figures for  $\text{tr } \mathbf{A}$ , with the horizontal streaks selected. This tells us that the interfaces are predominantly parallel to the material streaks. The comparisons for other components of the area tensor are quite similar, and are not shown here. A close match on all components of the area tensor indicate that the mapping method has correctly found the orientation of the interfaces, as well as their magnitude. Both mapping and tracking indicate that the distribution of interfacial area over the flow domain is noticeably less uniform than the concentration distribution, even at this early stage of mixing.

As a more quantitative measure, we can compare the total interfacial length  $L$  for the two methods. This is available directly for the interface tracking method, and for the mapping method it is simply the sum of the interfacial area among all the cells,  $L = \sum_i^N (\text{tr } \mathbf{A}_i) \Omega_i$ . In this particular case, when the marker fluid was initially centered around a hyperbolic point, the mapping approach describes the interfacial area generation quite accurately:  $L = 1231.5$  for interface tracking and 1278.6 for mapping, a difference of less than 3.7%. Note that this corresponds to stretching the initial interface by a factor of 925.4. We will see later that for arbitrary initial conditions the extended mapping method tends to overestimate the interfacial area, while predicting well its relative distribution.

## 4.2. Examples

To demonstrate the extended mapping approach we consider two mixing flows described by the same TB protocol but with different wall displacements. The flow with the dimensionless displacement  $D = 8$  has a large island, while the flow with  $D = 16$  can, for present purposes, be regarded as globally chaotic. Figs. 4(a) and (b) show the results of the analysis using the traditional tool of Poincaré maps which are used here for comparison.

Note that both Poincaré maps reveal the zones of chaotic mixing, where material is being stretched exponentially with time, and Fig. 4(a) shows zones of regular motion, where stretching is at best linear. However the Poincaré maps do not provide information on the actual concentration and amount of stretching, nor on the rate of change of these quantities.

Figs. 4(c) and (d) show the concentration distributions created by these two flows after eight periods for  $D = 8$ , and four periods for  $D = 16$ , as predicted by the original mapping method. The cavity is initially filled with white fluid in the left half and black fluid in the right half (this is the case in all further results unless stated otherwise). Different numbers of periods are used for the two protocols, so that both flows will have the same energy input, which is proportional to total wall displacement. The influence of the island is clearly visible for  $D = 8$ , while for  $D = 16$  the mixture is much more uniform.

Figs. 5(a), (c), and (e) show how mixing progresses with time for  $D = 16$ . For this chaotic protocol, the striation thickness of the emerging lamellar mixture pattern quickly become too fine to resolve with the basic mapping technique. Intrinsic numerical errors, caused by averaging on the cell scale at every mapping step, also tend to erase the fine structure of the mixture. As a result,

after only a few periods the computed concentration distribution is nearly uniform (Fig. 5(e)). This is a desirable mixing result on the macroscale, but in Fig. 5(e) the pattern of cell concentrations no longer reveals anything useful about the state of the mixture.

The extended mapping method compensates for this loss of information by tracking the microstructure within each cell. These results are shown in Figs. 5(b), (d) and (f). Here we show the values of  $\log(\text{tr} \mathbf{A})$  within each cell, for different times during the mixing process. A logarithmic scale is used because the area tensor distribution is very non-uniform. (Zero values of  $\text{tr} \mathbf{A}$ , present in the initial stage of mixing, are replaced by a small fictitious constant to permit the logarithmic plot.) Although the concentration distribution quickly becomes nearly uniform, the microstructure continues to evolve as mixing proceeds. In addition, the mixture remains highly structured at the microscale, and the interface distribution is highly non-uniform.

#### 4.3. Self-similarity of the microstructure

For the globally chaotic flow shown in Fig. 5, a self-similar pattern of interface distribution is established after a few periods. This behavior is well known for this type of flow and has been studied extensively by others (Muzzio et al., 1991; Alvarez et al., 1998; Giona et al., 1999, 2000). Here we want to show that the extended mapping method captures this behavior quite well. The pattern is maintained for all subsequent mixing, while the average value of the trace of the area tensor grows exponentially. Thus, Figs. 5(d) and (f) are identical in appearance, though the two

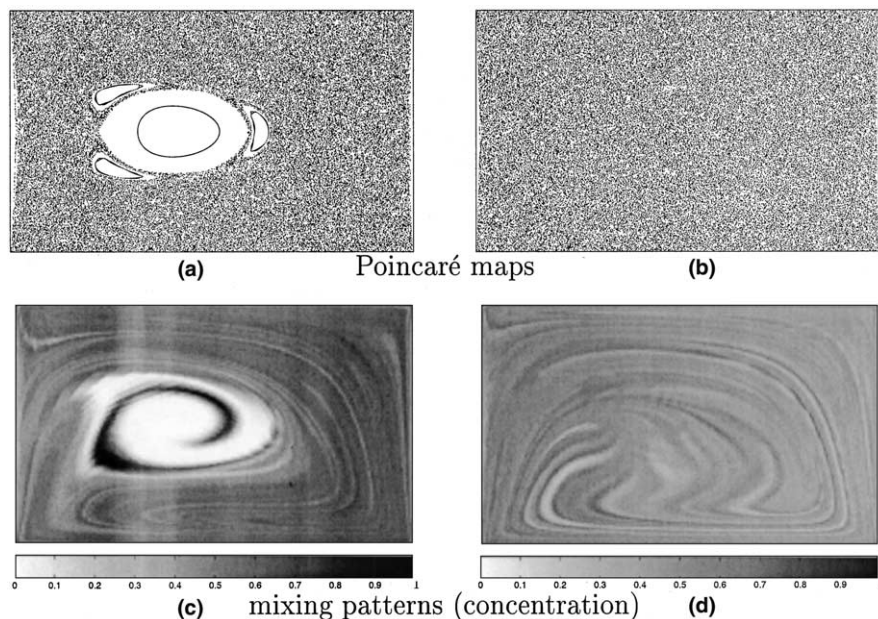


Fig. 4. Comparison of two flows with the TB protocol but different dimensionless wall displacement. The left column corresponds to the flow with  $D = 8$ , the right to the flow with  $D = 16$ : (a,b) Poincaré maps; (c,d) concentration distributions obtained using the mapping technique, after eight periods of the  $D = 8$  flow and four periods of  $D = 16$  flow, respectively.

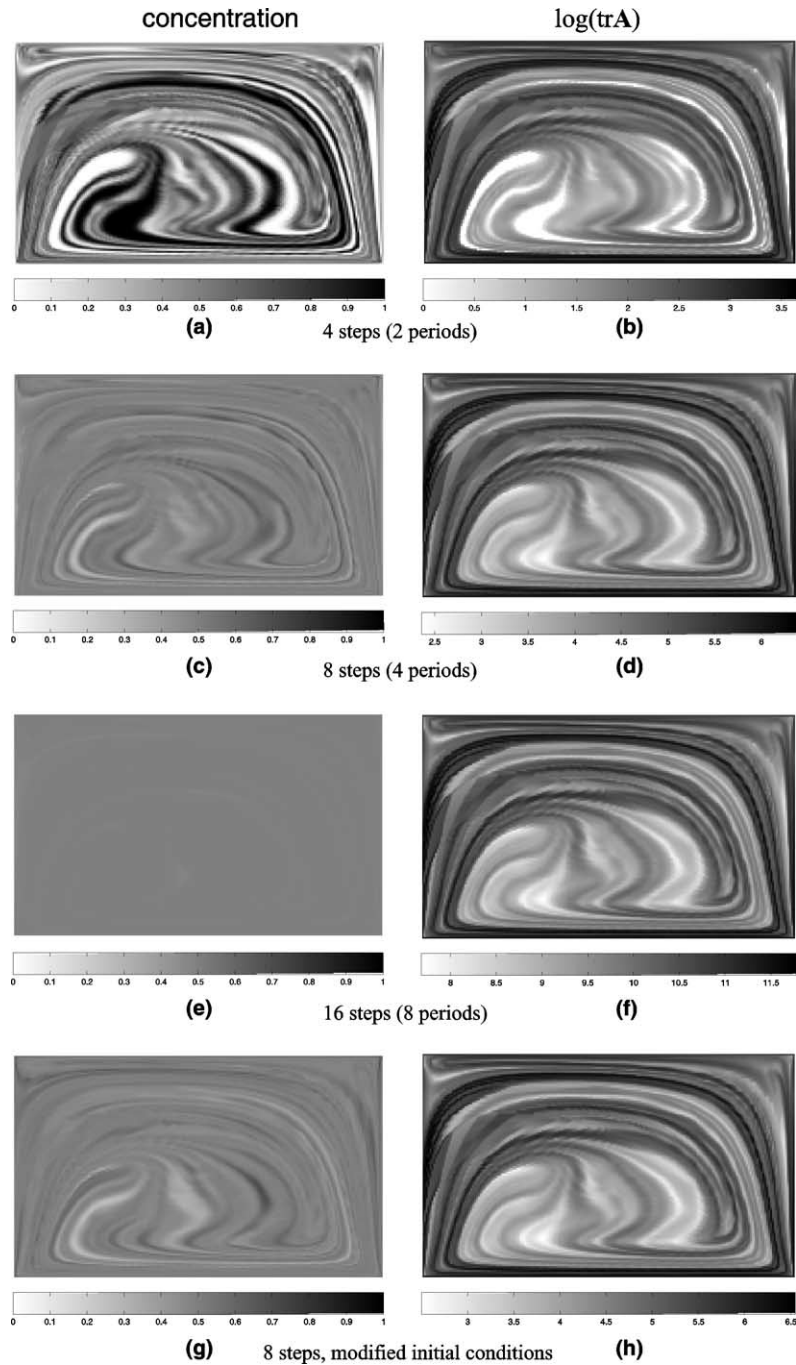


Fig. 5. (a–f) Evolution of concentration (left) and trace of the area tensor (right) distributions in the flow described by protocol TB with dimensionless displacement  $D = 16$ . Marker fluid initially fills the left half of the cavity. The results are shown after 2, 4, and 8 periods of the flow. (g,h): Similar to (c) and (d), but marker fluid initially fills the lower half of the cavity.

figures use different scales for their grey level maps. The pattern after only two periods, Fig. 5(b), is only slightly different from the self-similar pattern in Figs. 5(d) and (f).

For a globally chaotic flow, this self-similar pattern of the interface distribution is also independent of the initial configuration of the mixture. Figs. 5(g) and (h) show the distributions of concentration and of  $\text{tr} \mathbf{A}$  after four periods of the same flow, but for a different initial condition. Here the dark fluid initially occupies the lower half of the cavity, and the initial interface is horizontal. Although the concentration pattern in Fig. 5(g) is slightly different from Fig. 5(c), the interface distribution in Fig. 5(h) is identical to Fig. 5(d). The average value of  $\text{tr} \mathbf{A}$  in Fig. 5(h) is slightly higher than in the previous case, because the initial interface was longer.

This self-similarity of the interface distribution shows itself clearly in the statistics for the distribution of  $\text{tr} \mathbf{A}$ . Similar to the results of Liu et al. (1994b) for stretching statistics, and following Muzzio et al. (1991), we plot the probability density  $H_n$  as a function of  $\log(\text{tr} \mathbf{A})$ . This is computed as

$$H_n(\log(\text{tr} \mathbf{A})) = \frac{dN(\log(\text{tr} \mathbf{A}))}{d \log(\text{tr} \mathbf{A})}. \quad (22)$$

Here  $dN(\log(\text{tr} \mathbf{A}))$  is the number of cells with area tensor values in the range  $[\log(\text{tr} \mathbf{A}), \log(\text{tr} \mathbf{A}) + d \log(\text{tr} \mathbf{A})]$ .

Fig. 6 shows  $H_n$  computed after different numbers of periods for the TB flows, with  $D = 8$  and  $D = 16$ . In both cases the marker fluid initially filled the left half of the cavity. For the flow with  $D = 8$ , all curves in Fig. 6(a) show a long “tail” on the left, in the region of low values of  $\text{tr} \mathbf{A}$ . This tail corresponds to the large island in this flow, where interface generation is linear with time. The sharp peak at the left end of the curve represents the cells that contain no interface. (To allow logarithmic plots, values of  $\text{tr} \mathbf{A}$  that are smaller than one were replaced by one). The head of the curve, which corresponds to the region of chaotic mixing, quickly becomes self-similar, and the growth of interface in these cells is exponential with time.

The plots of  $H_n$  for the globally chaotic flow, with  $D = 16$ , are presented in Fig. 6(b). The number of periods for each curve is half the number for  $D = 8$  flow, so the energy inputs are the same between Fig. 6(a) and (b). For this globally chaotic flow the curves do not have tails at low  $\text{tr} \mathbf{A}$ , and the curves rapidly become self-similar. Despite the presence of a large island in the flow with  $D = 8$ , the values of  $\log(\text{tr} \mathbf{A})$  achieved in the head of the distribution curve for  $D = 8$  are higher than for the globally chaotic flow, with  $D = 16$ . However, the global properties of a mixture are usually governed by the location with the worst mixing, and in this respect the globally chaotic flow is far superior.

Once the self-similar pattern of microstructure is established, the amount of interfacial area grows exponentially. This is illustrated by the solid curve in Fig. 7. At each step during the calculation we find the total amount of interface in the entire mixture, computed as the sum over all cells of  $\text{tr} \mathbf{A}$  times the cell volume, normalized by the initial value. This is plotted in the figure as a function of the total wall displacement, for the chaotic flow ( $D = 16$ ). After the first period, the curve rises exponentially (becomes a straight line on this log/linear plot). Superimposed on this exponential rise is a ripple with half the period of the flow; this simply indicates that the growth of interface takes place non-uniformly over time within each period. The different curves in Fig. 7 correspond to calculations with different size mapping steps. This discrepancy in the interfacial area growth prediction is discussed in Section 4.5.

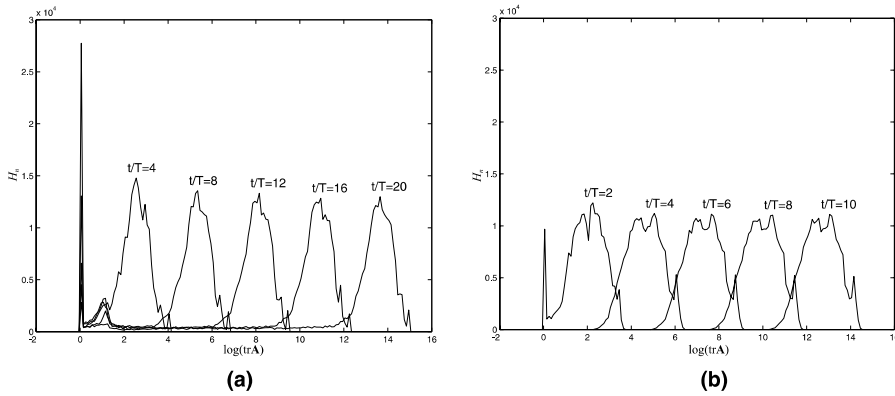


Fig. 6. Statistics of the interface distribution:  $H_n(\log(\text{tr } \mathbf{A}))$  for the TB flows with  $D = 8$  (a) and  $D = 16$  (b). The number of periods  $t/T$  is noted near each curve.

While the magnitude of the interfacial area grows exponentially for chaotic flows, the orientation and “shape” of the microstructure in each cell is periodic, and returns to a fixed value after each period of motion. Fig. 8 shows these orientation patterns for our two example flows. The length of each short dash is proportional to the difference between the maximum and minimum eigenvalues of  $\hat{\mathbf{A}} \equiv \mathbf{A}/\text{tr } \mathbf{A}$ , and the direction of the dash is perpendicular to the eigenvector associated with the largest eigenvalue. Thus, long dashes represent lamellar structures with the layer surfaces running parallel to the dash, while short dashes represent zones within which the interfaces are curved. Each dash in these figures represents the average area tensor is a square window of  $4 \times 4$  cells. This makes the results easier to see, though it does suppress some of the fine-scale information present in the data.

In Fig. 8 the orientation patterns are overlaid on the concentration distributions. It is apparent that both mixtures are, by this point, primarily lamellar in structure, and that the lamellae in each cell are oriented parallel to the streaks of fluid we see in the concentration patterns. Only a few cells, where the interfaces are folded with a radius of a few cell sizes or less, contain interfaces with different orientations, and appear as dots or very short dashes. Comparing Fig. 8(b) to Fig. 5(f) shows that, for the chaotic flow, the directionality of the microstructure also follows the shape of the streaks of high and low interfacial area. Note that this periodic orientation pattern for the microstructure also develops in the  $D = 8$  flow, even though this flow has large regular islands.

#### 4.4. Rate of interfacial area growth

We already examined the global rate of growth of interfacial area for a chaotic flow in Fig. 7. However, the extended mapping method can provide a more detailed analysis that reveals the spatial distribution of area stretching rates. Here we take advantage of the periodicity of the flow, and calculate the stretching for one period of the flow. This is done by providing an initial condition in which the trace of the initial area tensor  $\mathbf{A}^0$  equals unity for every cell, and then running the calculation for one period. The amount of stretching in each cell is computed as



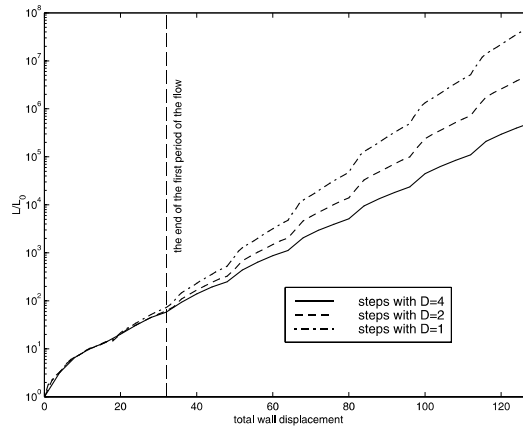


Fig. 7. The evolution of total interface length  $L/L_0$ , computed for the flow with protocol TB and dimensionless displacement  $D = 16$ , using different size mapping steps.

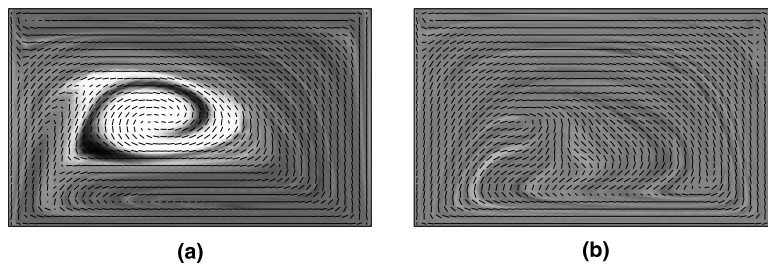


Fig. 8. Orientation patterns created by TB flows: (a)  $D = 8$ , background gray level corresponds to the concentration distribution after eight periods; (b)  $D = 16$ , background gray level corresponds to the concentration distribution after four periods.

$s = \text{tr} \mathbf{A} / \text{tr} \mathbf{A}^0$ . Thus, the stretch  $s$  in any cell is the factor by which the interfacial area increases during one period, for material that resides in that cell at the end of the period.

The orientation of the initial microstructure also affects the results, and here we examine two possibilities. The first is an isotropic initial state in every cell. This could occur, for instance, if the initial mixture consisted of small spherical droplets that were evenly distributed throughout the cavity. Results for this initial condition give an idea of which parts of the fluid experience large or small amounts of stretching during one period. The second possibility, which we call an oriented initial state, uses the interfacial orientation pattern created by the periodic flow. To create this initial condition we run the calculation for enough cycles to create a self-similar orientation pattern like those shown in Fig. 8, then normalize the orientation tensor in each cell so that it has unit trace. Calculating one additional period with this initial condition provides the values of  $s$  for the oriented initial state.

Fig. 9 shows the one-period stretching distributions for the flow with  $D = 8$ . The stretch values vary widely across the cavity, and we plot  $\log s$  to make the smaller values more visible. For the isotropic initial pattern, Fig. 9(a), we have  $\log s \geq 0$  (or  $s \geq 1$ ) in every cell. This behavior is

guaranteed, since there is no way to deform a region with isotropically distributed interfaces without stretching the interface. However, some cells in Fig. 9(a) stretch by less than 1%, while others stretch to more than 200 times their original value. Not surprisingly, the large island in this flow is a region with very little stretching. However, there are other regions of low stretching that exist as thin streaks, immediately adjacent to regions of very high stretch.

When the calculation is repeated with an oriented initial state, we find large stretching values in essentially the same places, but we also find significant regions where  $s < 1$ , or  $\log s < 0$ . These are outlined in white in Fig. 9(b). This might be called *microstructural demixing*. In these cells the interfaces have *less* area than they did at the beginning of the period. Demixing occurs when the initial interface is oriented unfavorably with respect to the deformation, and is only possible when the initial microstructure has some preferred orientation. The island contains some of these areas, but others exist in the chaotic region of the flow.

The stretching results for the globally chaotic flow, with  $D = 16$ , are shown in Fig. 10. The results are similar to the previous figure, with a wide range of values present, and thin streaks of low stretching lying alongside streaks of high stretching. In comparing Fig. 10(a) with the concentration pattern, Fig. 4(d), we see that the areas of small stretching are precisely the areas where striations are still visible in the concentration pattern after four periods.

For the oriented initial pattern in Fig. 10(b) the areas with  $s < 1$  are smaller than in the other flow, but demixing is still present. This raises an interesting question: if the one-period dynamics shows some demixing, why do the statistics for  $H_n$  in Fig. 6(b) show that the amount of interface in every cell increases for every period? The answer is that area growth depends on transport as well as stretching. Once the chaotic flow has established its self-similar pattern, material arriving in the “demixing” zones already has a higher-than average amount of interfacial area. The amount of demixing is less than the stretching that occurs elsewhere, and in the next period this material moves to some other location and experiences an increase in interfacial area. In calculations for time-periodic flows between eccentric cylinders, as studied by Muzzio et al. (1991) and Giona et al. (1999), we have detected even stronger demixing zones, where the interfacial area decreased by factors as large as 6–9 in a single period (Anderson et al., to appear). Interestingly, the flow with the largest contraction of area and the largest demixing zones showed the highest average stretching.

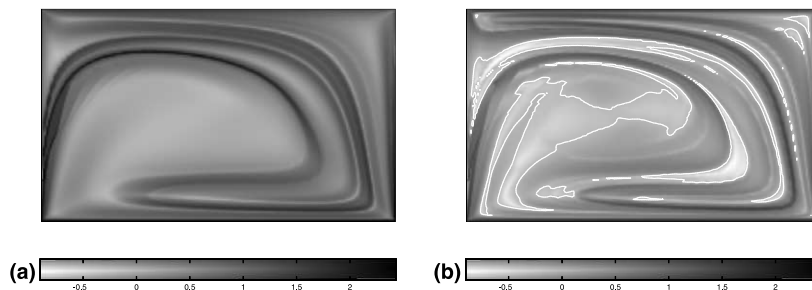


Fig. 9. One-period stretching distributions for  $D = 8$ : (a) for an isotropic initial pattern ( $0.0014 < \log s < 2.432$ ); (b) for an oriented initial pattern ( $-0.902 < \log s < 2.031$ ).

#### 4.5. Artifacts of the numerical method

The verification example presented at the beginning of this section showed that the extended mapping method somewhat overestimated the length of the interface. Furthermore, the results of Fig. 7 show that the calculated interfacial area in fact depends on the size of the mapping step used in the calculation. In this figure the total interface length in the cavity is plotted as a function of total displacement of the moving walls, but the three different curves accomplish this displacement using different mapping data. For instance, the curve labelled  $D = 4$  accomplishes the total displacement of the top wall,  $D = 16$ , using four mapping steps, while the curve labelled  $D = 1$  uses 16 mapping steps with a different mapping matrix and  $\mathbf{F}_{ij}^{-1}$  values to reach the same point. All three curves show an exponential rise in the interfacial area after the first period, but the rise rate increases as the size of the individual mapping steps decreases.

This over-prediction of interfacial area growth is closely related to the presence of the corner singularities in the velocity field. Although we do not cover the thin outer layer with the sub-domain grid, the deformation of material travelling close to the corner point is overestimated. The averaging in the long thin “boundary cell” (see Section 3.3) amplifies the effect. In calculations on physically realizable flows *without* singularities in the velocity field (Anderson et al., to appear), we find that length of the mapping step has a negligible influence on the predicted interfacial area growth.

The effect of “numerical diffusion” mentioned in Section 2.1, caused by the averaging process within each cell, can be demonstrated by transporting the concentration only, using Eq. (2). Fig. 11 shows one example. We consider a square domain, divided into  $50 \times 50$  cells. The initial pattern is white with a black vertical strip, one cell wide, in the center (Fig. 11(a)).

We first subject this to a horizontal translation, with a displacement of one half cell per mapping step. Fig. 11(b) shows the concentration pattern after three mapping steps. The strip of black fluid has translated, but has also become wider and more diffuse. Executing the reverse mapping on this pattern does not recover the initial state in Fig. 11(a), but gives Fig. 11(c), which is considerably more diffuse. Fig. 11(c) shows the spread in concentration of this recovered pattern. It also shows that the same calculation with five times more mapping steps gives yet more diffusion.

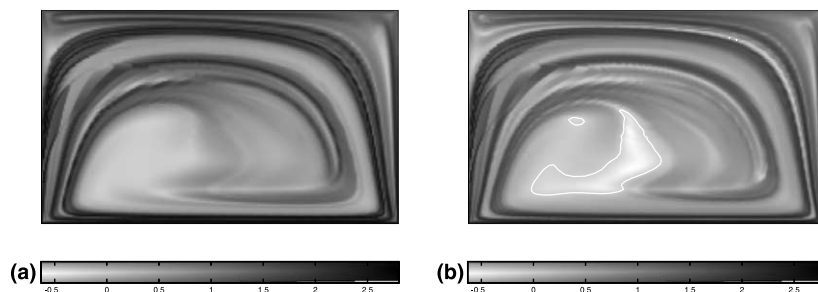


Fig. 10. One-period stretching distributions for  $D = 16$ : (a) for an isotropic initial pattern ( $0.0016 < \log s < 2.801$ ); (b) for an oriented initial pattern ( $-0.631 < \log s < 2.471$ ).

Note that this example is the worst case, since translating the pattern by integer number of cell sizes does not introduce any numerical diffusion. The numerical diffusion primarily spreads the mapped quantity (e.g., concentration) in the direction of the flow. In this example the non-zero concentration remains confined to the horizontal band of cells that contains the initial strip. (This band is marked with dashed lines in the figure.) However, if the flow direction is not aligned along the rows or columns of cells, the concentration will also spread sideways.

While the extended mapping method tends to over-predict the total interfacial area, the spatial distribution of interface within the cavity (i.e., the locations of the maxima and minima of  $\text{tr } \mathbf{A}$ ) are essentially independent of the size of the mapping step. Similarly, the pattern of spatial orientation is not greatly affected by the size of the mapping step.

Numerical artifacts can be minimized by using large-displacement mapping steps. However, the cost of the interface tracking calculation, which is used to find the mapping matrix  $[\Psi]$  and the  $\mathbf{F}_{ij}^{-1}$  values, grows exponentially with the size of the mapping step. Thus, it is not possible to use mapping steps that are much larger than the ones used here.

## 5. Summary

We have developed a simulation of laminar mixing that is global, in the sense that it treats the entire mixture, and that represents both the macroscopic and the microscopic aspects of mixing.

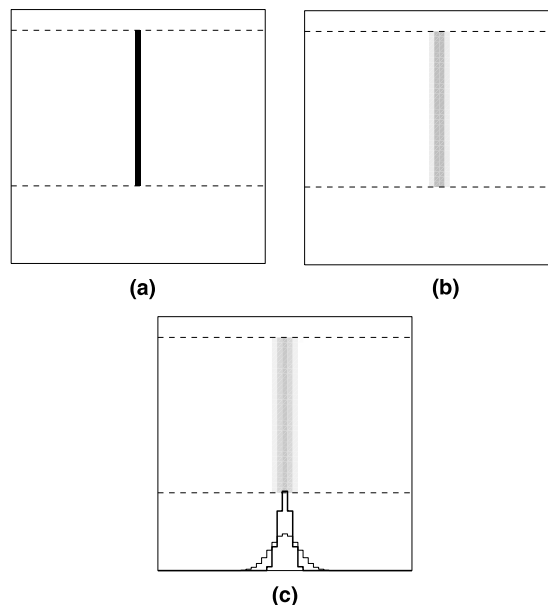


Fig. 11. Numerical artifacts of mapping demonstrated in a translational flow: (a) initial configuration, with vertical strip of marker fluid; (b) strip after three mappings, each corresponding to a translation of one half cell to the right; (c) recovery of the vertical strip by backward mapping. Thick line shows the concentration profile across the strip. Thin line shows the concentration profile for the strip recovered for an initial mapping that is five times larger.

At the macroscopic level one is concerned primarily with achieving an even distribution of the components throughout the mixture, and we track this using cell-average values of concentration. At the microscopic level the primary interest is the creation of a desirable microstructure, and this is followed by calculating an area tensor for each cell. The area tensor can represent the quantity, shape, and orientation of the interfaces contained within a cell, so it provides a useful tool for treating sub-grid scale information in laminar mixing.

The strength of the extended mapping method is that it models mixing directly. One can specify the initial configuration of the two fluids, subject them to a prescribed amount of mixing, and predict the concentration and microstructure distributions at every point in the resulting mixture. Thus, there is no need to resort to any correlation between properties of the flow and properties of the mixture. The extended mapping method correctly reflects the spatial self-similarity and exponential interface growth that occurs at long times in chaotic flows, but it can also predict short-time behavior of chaotic flows, as well as the mixing in regular regions.

We can contrast this to various tools that have been used to analyze laminar mixing. Total strain, or total work done on the fluid, is one of the oldest measures of mixing, but it ignores important factors: the orientation of the interfaces relative to the deformation, the initial configuration of the fluids, and the possibility of regular islands in the flow. The two TB cavity flows examined here were compared at identical values of total strain, but provided very different mixing results. Poincaré maps reveal regular islands and chaotic regions, but do not provide any information about interfacial area or stretching. Periodic point analysis will locate the points of greatest and least stretching efficiency (the hyperbolic and elliptic points, respectively), but one gains insight primarily into the local behavior around these points. Stretching distributions provide information that is much closer to our microstructural results, but they are not usually computed for a practical initial condition, and they do not treat the distributive aspects of mixing. The extended mapping calculation provides a complete treatment of mixing, focusing on the information needed to select mixing devices and design mixing processes.

The extended mapping method can readily be applied to 3D flows, unstructured grids, and flows of generalized Newtonian fluids (Anderson et al., 2000, to appear; Galaktionov et al., 2001, 2000b; Kruijt et al., 2001b,c). However, mixtures of fluids with unequal viscosities, interfacial tension, viscoelastic properties, or diffusing and reacting species cannot be treated rigorously, unless one makes some significant extensions or alterations to the method. We expect these phenomena can be incorporated into global, multi-scale models of mixing, albeit with more complex models and different numerical methods.

## Acknowledgements

Financial support for this work was provided by the Dutch Technology Foundation STW, grant number EWT.44.3453, and by the National Science Foundation, grant number DMI 98-13020. Charles Tucker gratefully acknowledges financial support from the Dutch Polymer Institute for his stay at the Eindhoven University of Technology. The authors also thank Dr. Eric D. Wetzel of the Army Research Laboratory, Aberdeen, Maryland, for helpful discussions of the area and shape tensors.

## Appendix A. Intersecting areas of enclosed polygons

To compute the elements of the mapping matrix, we must compute the intersections between the deformed sub-domains, which were tracked in the flow, and the grid of initial sub-domains. The boundaries of both deformed and undeformed sub-domains are represented by closed polygons. Mathematically, the problem is reduced to finding the intersection of the areas enclosed by two polygons.

In this work we use a simple and general algorithm, which is able to find these intersection areas exactly. The only essential requirement is that each polygon be closed and not self-intersecting. This will always be true if each polygon is the boundary of a material domain. Fig. 12 illustrates the steps of the algorithm.

First, we find all intersections of the edges of the first polygon with edges of the second polygon. At these points, additional vertices are added to both polygons, splitting these edges. Now the modified polygons intersect only at their vertices (see Fig. 12(b)). Second, the boundary of the intersection area is formed as shown in Fig. 12(c). The edges of the intersection area are the edges from the first modified polygon that are located inside the second polygon, and the edges of the second polygon that are located inside the first polygon. Because the polygons now intersect only at their vertices, one can easily decide if certain edge lies inside another polygon by checking its midpoint. The intersection between two polygons can, in general, consist of non-connected parts, as illustrated in Fig. 12(c). Our algorithm handles these cases correctly. However, in mapping computations the sub-domains are usually small, so multi-part intersections are rare.

## Appendix B. Numerical evaluation of $F^{-1}$

The extended mapping technique requires us to find the deformation gradient tensor relating the original and deformed configurations, for the material in any deformed cell that intersects an undeformed cell. The intersecting area is represented by a closed polygon, as described in Appendix A. To begin, the position  $p'_0$  of the center of mass of this intersection is calculated. We assume that the cells are sufficiently small that the deformation of all the material within the cell can be described by the value at the center of mass. To evaluate the deformation gradient, the point  $p'_0(x'_0, y'_0)$  is surrounded by the cross-like stencil of four points, shifted along the  $x$ - or  $y$ -axis by a small distance  $d$ :  $p'_1(x'_0 + d, y'_0)$ ,  $p'_2(x'_0, y'_0 + d)$ ,  $p'_3(x'_0 - d, y'_0)$ ,  $p'_4(x'_0, y'_0 - d)$ . Next, these points are tracked in from  $t = t_0 + \Delta t$  back to their initial positions  $p_1(x_1, y_1)$ ,  $p_2(x_2, y_2)$ ,  $p_3(x_3, y_3)$ ,

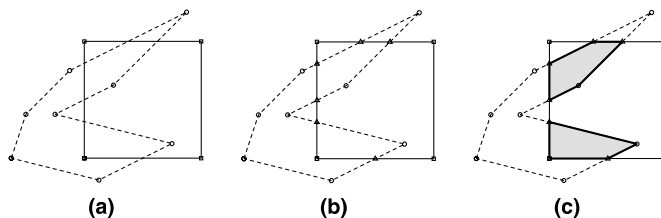


Fig. 12. Finding the intersection of the area enclosed by two closed polygons: (a) initial polygons; (b) extra vertices are added where the polygons intersect, splitting these sides; (c) the boundary of the intersecting area is then determined.

$p_4(x_4, y_4)$  at  $t = t_0$ , using the kinematics of the flow field (Fig. 13). Finally, the components of the inverse deformation gradient tensor  $\mathbf{F}^{-1}$  are evaluated using a central finite difference scheme:

$$\mathbf{F}^{-1} = \begin{pmatrix} \frac{\partial x}{\partial x'} & \frac{\partial x}{\partial y'} \\ \frac{\partial y}{\partial x'} & \frac{\partial y}{\partial y'} \end{pmatrix} \approx \begin{pmatrix} \frac{x_1 - x_3}{x'_1 - x'_3} & \frac{x_2 - x_4}{y'_2 - y'_4} \\ \frac{y_1 - y_3}{x'_1 - x'_3} & \frac{y_2 - y_4}{y'_2 - y'_4} \end{pmatrix} = \frac{1}{2d} \begin{pmatrix} x_1 - x_3 & x_2 - x_4 \\ y_1 - y_3 & y_2 - y_4 \end{pmatrix}. \tag{B.1}$$

This procedure is carried out for each non-zero entry  $\Psi_{ij}$  in the mapping matrix, producing the values  $\mathbf{F}^{-1}_{ij}$ .

### Appendix C. Converting between area tensors and droplet shape tensors

To transform the area tensor under finite strain, we must convert from the area tensor to the shape tensor for equivalent ellipsoidal droplets, and back again. This appendix shows the details of that conversion.

With the area tensor, the length scale of the microstructure is determined by the trace of the tensor, which equals the interfacial area per unit volume  $S_V$  (Eq. (6)). The “shape” of the tensor is described by the normalized area tensor  $\hat{\mathbf{A}}$ , defined as

$$\hat{\mathbf{A}} \equiv \frac{\mathbf{A}}{S_V}. \tag{C.1}$$

The droplet shape tensor  $\mathbf{G}$ , defined in Eq. (14), describes the shape and size of identical ellipsoidal droplets. Initially we choose coordinate axes that coincide with the symmetry axes of the ellipsoid. These are the eigenvectors of the tensor  $\mathbf{G}$ . Let the semi-axes of the droplet be  $a$ ,  $b$ , and  $c$ , with  $a \geq b \geq c$ . We number the axes so that the droplet shape tensor is

$$\mathbf{G} = \begin{bmatrix} 1/c^2 & 0 & 0 \\ 0 & 1/b^2 & 0 \\ 0 & 0 & 1/a^2 \end{bmatrix}. \tag{C.2}$$

The shape of the droplet is described by the two axis ratios

$$C = \frac{c}{a}, \quad D = \frac{c}{b}. \tag{C.3}$$

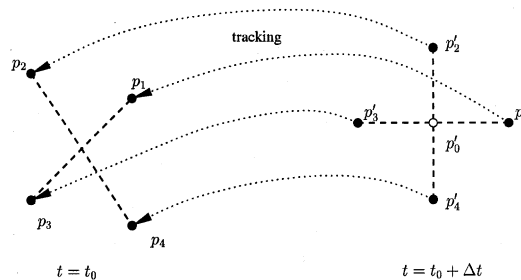


Fig. 13. Numerical evaluation of  $\mathbf{F}^{-1}$ : the points of a cross-shaped stencil are tracked from time  $t = t_0 + \Delta t$  back to  $t = t_0$ .

Note that both  $C$  and  $D \in [0, 1]$ . Once  $C$  and  $D$  are known, the droplet size is determined by specifying  $c$ .

One can establish the correspondence between  $\mathbf{A}$  and  $\mathbf{G}$  for ellipsoidal droplets by evaluating the integral in Eq. (5) over the surface of an ellipsoid. The two tensors are coaxial, so if the shape tensor is diagonal as in Eq. (C.2), the area tensor will also be diagonal.

The normalized area tensor  $\hat{\mathbf{A}}$  depends only on the axis ratios  $C$  and  $D$ , and the exact relationships have been derived by Wetzel and Tucker (1999) and Wetzel (1999). They are

$$\hat{A}_{11} = \frac{1}{1 - D^2} \frac{E(\theta, k) - D^2 F(\theta, k)}{(1 - C^2)E(\theta, k) + C^2 F(\theta, k) + CD\sqrt{1 - C^2}}, \quad (\text{C.4})$$

$$\hat{A}_{22} = \frac{D^2}{D^2 - C^2} \times \frac{\{(D^2 - C^2)/(1 - D^2)\}F(\theta, k) - D^2\{(1 - C^2)/(1 - D^2)\}E(\theta, k) + CD\sqrt{1 - C^2}}{(1 - C^2)E(\theta, k) + C^2 F(\theta, k) + CD\sqrt{1 - C^2}}, \quad (\text{C.5})$$

$$\hat{A}_{33} = \frac{C^2}{D^2 - C^2} \frac{C^2 E(\theta, k) + (D^2 - C^2)F(\theta, k) - CD\sqrt{1 - C^2}}{(1 - C^2)E(\theta, k) + C^2 F(\theta, k) + CD\sqrt{1 - C^2}}, \quad (\text{C.6})$$

where  $F(\theta, k)$  and  $E(\theta, k)$  are the Legendre elliptic integrals of the first and second kind, respectively (Gradshteyn and Ryzhik, 1994), and  $k$  and  $\theta$  are

$$k = \sqrt{\frac{1 - D^2}{1 - C^2}}, \quad \theta = \cos^{-1}(C). \quad (\text{C.7})$$

These exact relationships cannot be inverted analytically, and an iterative numerical procedure is required. As an alternative, Wetzel and Tucker (1999) found that these relationships are well approximated by

$$C \cong \left( \frac{\hat{A}_{33}}{\hat{A}_{11}} \right)^\alpha, \quad D \cong \left( \frac{\hat{A}_{22}}{\hat{A}_{11}} \right)^\alpha \quad (\text{C.8})$$

with  $\alpha = 0.5977$ . The semi-axis ratio values from this approximation are exact for the limiting cases of uniaxial, biaxial, and isotropic tensors, and they fall within 0.04 of the exact values for all other ellipsoidal shapes. Eqs. (C.8) can be inverted analytically, to give

$$\hat{A}_{11} \cong \frac{1}{(c/a)^{1/\alpha} + (c/b)^{1/\alpha} + (c/c)^{1/\alpha}} = \frac{1}{(C)^{1/\alpha} + (D)^{1/\alpha} + 1}, \quad (\text{C.9})$$

$$\hat{A}_{22} \cong \frac{1}{(b/a)^{1/\alpha} + (b/b)^{1/\alpha} + (b/c)^{1/\alpha}} = \frac{1}{(C/D)^{1/\alpha} + 1 + (1/D)^{1/\alpha}}, \quad (\text{C.10})$$

$$\hat{A}_{33} \cong \frac{1}{(a/a)^{1/\alpha} + (a/b)^{1/\alpha} + (a/c)^{1/\alpha}} = 1 - \hat{A}_{11} - \hat{A}_{22}. \quad (\text{C.11})$$

This is the form used for the calculations in this paper. By definition  $\hat{A}_{11} + \hat{A}_{22} + \hat{A}_{33} = 1$ , so there are only two independent eigenvalues of the normalized area tensor. Either Eqs. (C.4)–(C.6) or



Eqs. (C.8)–(C.11) provide the mapping between the axis ratios  $C$  and  $D$  and these two components.

To complete the relationship, we must also relate the “sizes” of the two tensors. This is determined from the surface area to volume ratio. The volume of the ellipsoid is

$$V_e = \frac{4}{3}\pi abc \quad (\text{C.12})$$

while its exact surface area is

$$S_e = 2\pi c^2 \left( 1 + \frac{\sqrt{1-C^2}}{CD} E(\theta, k) + \frac{C}{D\sqrt{1-C^2}} F(\theta, k) \right). \quad (\text{C.13})$$

A convenient approximation to the surface area that avoids the elliptic integral functions  $F$  and  $E$  is (Lehmer, 1950)

$$S_e \cong 4\pi ab \left( \frac{2}{5} \frac{C+D+1}{3} + \frac{3}{5} \sqrt{\frac{C^2+D^2+1}{3}} \right). \quad (\text{C.14})$$

If the ellipsoidal droplets occupy a fraction  $\phi$  of the mixture volume, then their surface area per unit total volume is

$$S_V = \frac{\phi S_e}{V_e}. \quad (\text{C.15})$$

Substituting the exact area formula (C.13) and the volume (C.12), we find

$$S_V = \frac{3\phi c}{2ab} \left[ 1 + \frac{\sqrt{1-C^2}}{CD} E(\theta, k) + \frac{C}{D\sqrt{1-C^2}} F(\theta, k) \right]. \quad (\text{C.16})$$

For numerical calculations it is useful to rearrange this formula as

$$S_V = \frac{3\phi}{2c} \left[ CD + \sqrt{1-C^2} E(\theta, k) + \frac{C^2}{\sqrt{1-C^2}} F(\theta, k) \right]. \quad (\text{C.17})$$

This handles the case where  $a \rightarrow \infty$  and  $C \rightarrow 0$  smoothly, and also has no problems if in addition  $b \rightarrow \infty$  and  $D \rightarrow 0$ .

Alternately, one can use the approximate area formula (C.14), in which case

$$S_V \cong \frac{\phi}{c} \left[ \frac{2}{5} (C+D+1) + \frac{3}{5} \sqrt{3(C^2+D^2+1)} \right]. \quad (\text{C.18})$$

In either case we have a direct relationship between  $S_V$  and  $c$ .

We now have all the pieces needed transform between the area tensor and the droplet shape tensor. To go from  $\mathbf{G}$  to  $\mathbf{A}$  the algorithm is:

- (i) Find the eigenvalues and eigenvectors of  $\mathbf{G}$ . The eigenvalues give  $a$ ,  $b$ , and  $c$  according to Eq. (C.2). Normalize the eigenvectors and use them to form the rotation matrix  $\mathbf{R}$  between the principal axes and the laboratory axes. Compute  $C$  and  $D$  from Eq. (C.3).

- (ii) Determine the principal components of the normalized area tensor  $\hat{\mathbf{A}}$ , using either the exact relations (C.4)–(C.6) or the approximate relations (C.9)–(C.11).
- (iii) Determine  $S_V$  using either the exact formula (C.16) or the approximate formula (C.18).
- (iv) Compute the area tensor in its principal coordinates using Eq. (C.1), i.e.  $\mathbf{A} = S_V \hat{\mathbf{A}}$ .
- (v) Use  $\mathbf{R}$  from the first step to rotate  $\mathbf{A}$  back to the laboratory axis system.

The reverse transformation, from  $\mathbf{A}$  to  $\mathbf{G}$ , follows a similar pattern. If the exact shape formulae (C.4)–(C.6) are used, then an iterative numerical procedure is required to find  $C$  and  $D$ . The approximate formulae can be used to provide a close initial guess, after which a Newton–Raphson iteration should converge without difficulty.

## References

- Alvarez, M.M., Muzzio, F.J., Cerbelli, S., Adrover, A., Giona, M., 1998. Self-similar spatiotemporal structure of intermaterial boundaries in chaotic flows. *Phys. Rev. Lett.* 81, 3395–3398.
- Anderson, P., Galaktionov, O., Peters, G., van de Vosse, F., Meijer, H., 2000. Chaotic fluid mixing in non-quasi-static time-periodic cavity flows. *Int. J. Numer. Meth. Heat Fluid Flow* 21, 176–185.
- Anderson, P.D., Galaktionov, O.S., Peters, G.W.M., Meijer, H.E.H., Tucker, C.L., to appear. Material stretching in laminar mixing flows: extended mapping technique applied to the journal bearing flow. *J. Non-Newtonian. Fluid Mech.*
- Aref, H., 1984. Stirring by chaotic advection. *J. Fluid Mech.* 143, 1–21.
- Aref, H., Balachandar, S., 1986. Chaotic advection in a Stokes flow. *Phys. Fluids* 29, 3515–3521.
- Batchelor, G.K., 1970. The stress system in a suspension of force-free particles. *J. Fluid Mech.* 41, 545–570.
- Chien, W.-L., Rising, H., Ottino, J.M., 1986. Laminar mixing and chaotic mixing in several cavity flows. *J. Fluid Mech.* 170, 355–377.
- Doi, M., Ohta, T., 1991. Dynamics and rheology of complex interfaces I. *J. Chem. Phys.* 95, 1242–1248.
- Franjione, J., Leong, C., Ottino, J., 1989. Symmetries within chaos: A route to effective mixing. *Phys. Fluids A* 1 (11), 1772–1783.
- Galaktionov, O.S., Anderson, P.D., Kruijt, P.G.M., Peters, G.W.M., Meijer, H.E.H., 2001. An mapping approach for three-dimensional distributive mixing analysis. *Comput. Fluids* 30, 271–289.
- Galaktionov, O.S., Anderson, P.D., Peters, G.W.M., van de Vosse, F.N., 2000a. An adaptive front tracking technique for three-dimensional transient flows. *Int. J. Numer. Meth. Fluids* 32, 201–218.
- Galaktionov, O.S., Kruijt, P.G.M., Anderson, P.D., Peters, G.W.M., Meijer, H.E.H., 2000b. Numerical simulations of fluid mixing and optimization of mixers. In: *Proceedings of SGI-2000. Krakow, Poland*, pp. 469–471.
- Giona, M., Adrover, A., Muzzio, F.J., Cerbelli, S., 2000. The geometry of mixing in 2-D time-periodic chaotic flows. *Chem. Eng. Sci.* 55, 381–389.
- Giona, M., Adrover, A., Muzzio, F.J., Cerbelli, S., Alvarez, M.M., 1999. The geometry of mixing in time-periodic chaotic flows. I. Asymptotic directionality in physically realizable flows and global invariant properties. *Phys. D* 132, 298–324.
- Gradshteyn, I.S., Ryzhik, I.M., 1994. *Table of Integrals, Series, and Products*, fifth ed. Academic Press, New York.
- Grmela, M., Ait-Kadi, A., 1998. Rheology of inhomogeneous immiscible blends. *J. Non-Newtonian Fluid Mech.* 77, 191–199.
- Khakhar, D., Rising, H., Ottino, J., 1986. Analysis of chaotic mixing in two model systems. *J. Fluid Mech.* 172, 419–451.
- Kruijt, P., 2000. Analysis and optimization of laminar mixing (design, development and application of the mapping method). Ph.D. thesis, Eindhoven University of Technology, The Netherlands.
- Kruijt, P.G.M., Galaktionov, O.S., Anderson, P.D., Peters, G.W.M., Meijer, H.E.H., 2001a. Analyzing fluid mixing in periodic flows by distribution matrices: Mapping method. *AIChE J.* 47, 1005–1015.

- Kruijt, P.G.M., Galaktionov, O.S., Peters, G.W.M., Meijer, H.E.H., 2001b. The mapping method for mixing optimization. Part I: The multiflux static mixer. *Int. Polym. Proc.* 16, 151–160.
- Kruijt, P.G.M., Galaktionov, O.S., Peters, G.W.M., Meijer, H.E.H., 2001c. The mapping method for mixing optimization. Part II: Transport in a corotating twin screw extruder. *Int. Polym. Proc.* 16, 161–171.
- Lehmer, D.H., 1950. Approximations to the area of an  $n$ -dimensional ellipsoid. *Can. J. Math.* 2, 267–282.
- Leong, C.W., Ottino, J.M., 1989. Experiments on mixing due to chaotic advection in a cavity. *J. Fluid Mech.* 209, 463–499.
- Liu, M., Muzzio, F.J., Peskin, R.L., 1994a. Quantification of mixing in aperiodic chaotic flows. *Chaos, Solitons & Fractals* 4, 869–893.
- Liu, M., Peshkin, R.L., Muzzio, F.J., Leong, C.W., 1994b. Structure of the stretching field in chaotic cavity flows. *AIChE J.* 40, 1273–1286.
- Meleshko, V.V., 1996. Steady Stokes flow in a rectangular cavity. *Proc. Roy. Soc. London A* 452, 1999–2002.
- Meleshko, V.V., Gomitko, A.M., 1997. Infinite systems for a biharmonic problem in a rectangle. *Proc. Roy. Soc. London A* 453, 2139–2160.
- Meleshko, V.V., Peters, G.W., 1996. Periodic points for two-dimensional Stokes flow in a rectangular cavity. *Phys. Lett. A* 216, 87–96.
- Mohr, W.D., Saxton, R.L., Jepson, C.H., 1957. Mixing in laminar-flow systems. *Ind. Eng. Chem.* 49, 1855–1856.
- Muzzio, F.J., Alvarez, M.M., Cerbelli, S., Giona, M., Adrover, A., 2000. The intermaterial area density generated by time- and spatially periodic 2-D chaotic flows. *Chem. Eng. Sci.* 55, 1497–1508.
- Muzzio, F.J., Swanson, P.D., Ottino, J.M., 1991. The statistics of stretching and stirring in chaotic flows. *Phys. Fluids* 3, 822–834.
- Onuki, A., 1987. Viscosity enhancement by domains in phase-separating fluids near the critical point: Proposal of critical rheology. *Phys. Rev. A* 35, 5149–5155.
- Ottino, J., 1989. *The Kinematics of Mixing: Stretching, Chaos and Transport*. Cambridge University Press, Cambridge.
- Peters, G.W.M., Hansen, S., Meijer, H.E.H., 2001. Constitutive modeling of dispersive mixtures. *J. Rheol.* 45, 659–689.
- Spencer, R.S., Wiley, R.H., 1951. The mixing of very viscous liquids. *J. Colloid Sci.* 6, 133–145.
- Swanson, P., Ottino, J., 1990. A comparative computational and experimental study of chaotic mixing of viscous fluids. *J. Fluid Mech.* 213.
- Tucker, C.L., Peters, G.W.M., submitted. Global measures of distributive mixing and their behavior in chaotic flows. *AIChE J.*
- Wagner, N.J., Öttinger, H.C., Edwards, B.J., 1999. Generalized Doi-Ohta model for multiphase flow developed via GENERIC. *AIChE J.* 45, 1169–1181.
- Wetzel, E.D., 1999. Modeling flow-induced microstructure in liquid–liquid mixing. Ph.D. thesis, University of Illinois at Urbana-Champaign, Urbana, IL.
- Wetzel, E.D., Tucker, C.L., 1999. Area tensors for modeling microstructure during laminar liquid–liquid mixing. *Int. J. Multiphase Flow* 25, 35–61.
- Wetzel, E.D., Tucker, C.L., 2001. Droplet deformation in dispersions with unequal viscosities and zero interfacial tension. *J. Fluid Mech.* 426, 199–228.